PHYSICAL REVIEW E, VOLUME 65, 046419

Parameters and equilibrium profiles for large-area surface-wave sustained plasmas

I. B. Denysenko,[1] A. V. Gapon,[1] N. A. Azarenkov,[1] K. N. Ostrikov,[2,3,4,5,*] and M. Y. Yu[5,†]
[1]*School of Physics and Technology, Kharkiv National University, 4 Svobody Square, 61077 Kharkiv, Ukraine*
[2]*Department of Electrical Engineering, Nagoya University, Furo-cho, Chikusa-ku, Nagoya 464-8603, Japan*
[3]*Plasma Sources and Applications Center, NIE, Nanyang Technological University, 1 Nanyang Walk, 637616 Singapore*
[4]*School of Chemistry, Physics and Earth Sciences, The Flinders University of South Australia, Adelaide, South Australia 5001, Australia*
[5]*Faculty of Physics and Astronomy, Ruhr University, 44780 Bochum, Germany*

(Received 12 February 2001; revised manuscript received 21 November 2001; published 11 April 2002)

The equilibrium profiles of the plasma parameters of large-area rf discharges in a finite-length metal-shielded dielectric cylinder are computed using a two-dimensional fluid code. The rf power is coupled to the plasma through edge-localized surface waves traveling in the azimuthal direction along the plasma edge. It is shown that self-consistent accounting for axial plasma diffusion and radial nonuniformity of the electron temperature can explain the frequently reported deviations of experimentally measured radial density profiles from that of the conventional linear diffusion models. The simulation results are in a good agreement with existing experimental data obtained from surface-wave sustained large-diameter plasmas.

DOI: 10.1103/PhysRevE.65.046419 PACS number(s): 52.80.−s, 52.25.−b, 52.50.−b

I. INTRODUCTION

The generation of high-density plasmas with large volumes has recently become a major concern in the semiconductor and other industries. In particular, fabrication of large-area semiconductor wafers, laser crystals, plasma displays, solar cells, as well as processing and modification of tools and materials, require substantial size up-scaling of existing discharge chambers. Of special interest is the cross section and volume uniformity of such large plasmas [1–3]. For this purpose rf low-pressure discharges in cylindrical vessels of large aspect ratio (LAR) are appropriate for use in future commercial large-area plasma processing facilities [4–8].

Several types of rf discharges, including inductively and capacitively coupled as well as (helicon or surface) wave driven, can be used for producing large-area and volume plasmas [9] for industrial use. In this paper, we investigate surface-wave (SW) sustained discharges with several distinct features. In particular, the SWs make use of the plasma and surrounding dielectric as a wave guiding structure with directional power flows localized near the plasma-dielectric interface [2]. Due to the enlarged power deposition area, the plasma can extend to far outside the field applicator region and can be remarkably large in volume and cross section [2]. Furthermore, SW sustained discharges have proven to be very flexible with respect to the operation parameters. They can be sustained for a remarkably wide regime of driver frequency, gas pressure, and composition, as well as plasma size. Various types of wave launchers and impedance matching schemes allow stable generation of SW plasmas in the frequency range from a few megahertz up to 40 GHz [2,10]. Meanwhile, the operating gas pressure can vary from fractions of millitorr to a few times atmospheric pressure [2,3].

Most earlier theoretical investigations on SW discharges are for long cylindrical plasma columns (see, e.g., [11–13] and references therein). The plasma is usually taken to be homogeneous in the axial direction, so that charged particle transport in that direction can be neglected. The radial plasma density profile in the diffusion-controlled discharge regime, as in most low-pressure discharges used in the applications, then obeys the well-known expression

$$n_e(r) \sim n_e(0) J_0(\beta r) \tag{1}$$

from the classical linear diffusion theory. Here, n_e is the electron number density and J_0 is the Bessel function of order zero. The constant β depends on the electromagnetic boundary conditions at the chamber wall [9]. For example, for $n_e(R)=0$ we have $\beta=\rho_{01}/R$, where $J_0(\rho_{01})=0$. However, significant deviation, such as a flattening of the profile (1) accompanied by a shift of the plasma density maximum away from the chamber axis, have been reported for many rf and microwave discharges at low pressures (see, e.g., [7,8,14,15]). The radial profile flattening is usually attributed to the intrinsic nonuniformity in power deposition and the action of the ponderomotive force [16,17].

For LAR discharges characterized by $R/L \sim 1$, where R and L are, respectively, the chamber radius and length, radial inhomogeneity and axial diffusion can be crucial [14]. In this paper we consider LAR rf discharges produced and sustained by SWs propagating azimuthally along the circumference of the plasma. We shall take into account self-consistently the radial variation of the electron temperature and hence also the nonuniformity of the (spatially distributed) ionization source. Axial electron and ion diffusion, as well as radial heat transport, usually neglected in unmagnetized SW discharge models, are also included. The problem of self-consistent particle and power balance is essentially nonlinear, and we shall adopt a numerical approach. Realistic density profiles for LAR cylindrical rf discharges are then obtained. It is shown that the results from our model agree

---

*Also at School of Electrical and Electronic Engineering, Nanyang Technological University, 639798 Singapore.
†Corresponding author.
Email address: yu@tp1.ruhr-uni-bochum.de

©2002 The American Physical Society

TABLE I. Main parameters and typical values.

Parameter	Notation	Value
Electron temperature	T_e	0.7–2.2 eV
Ion temperature	T_i	0.026 eV
Temperature of neutrals	T_n	0.026 eV
Gas pressure (Ar)	p_0	0.1–0.76 Torr
Plasma density	n	$10^8 - 10^{13}$ cm^{-3}
Absorbed RF power	Q	60–300 W
Tube dielectric constant	ε_d	4
Tube thickness	$b-a$	1.2 cm
Discharge length	L	5–15 cm
Discharge radius	a	6.3–10 cm
Wave frequency	$\omega/2\pi$	900 MHz and 2.45 GHz
Recombination coefficient	β	10^{-8} cm^3/s
Ionization threshold (Ar)	$\mathcal{E}_i$	15.76 eV
4s excitation threshold (Ar)	$\mathcal{E}_{4s}$	11.5 eV
4p excitation threshold (Ar)	$\mathcal{E}_{4p}$	13.2 eV
Ion mass (Ar)	m_i	$1836\times 40 m_e$
Radial fluid velocity	$\|v_r\|$	$(0-5)\times 10^5$ cm/s
Axial fluid velocity	$\|v_z\|$	$(0-1.5)\times 10^5$ cm/s

quite well with the experimental data, and that the radial plasma uniformity can be efficiently controlled by the operating gas pressure.

The paper is organized as follows. The problem is formulated in Sec. II. Section III deals with the method of the numerical solution. In Sec. IV, the profiles of the plasma parameters are computed for two different aspect ratios $R/L>1$ and $R/L\sim 1$. The results are then compared with available experimental data. In Sec. V the validity of our model and its results are discussed. A summary of this work is given in the last section. Table I lists the various parameters and typical values used in this paper.

II. FORMULATION

A. Basic assumptions

We consider an rf discharge in a cylindrical quartz tube with metal casing. The plasma is sustained by SWs traveling in the azimuthal (φ) direction along the edge of the cylinder. A sketch of the chamber is shown in Fig. 1, where a and b are the internal and external radii of the quartz tube, respectively. At $z=\pm L/2$ the plasma column is short circuited by metal plates. The wavelength λ and the penetration distance λ_s of the SWs are assumed to be small compared to the internal radius a of the chamber. The width of the near-wall plasma sheath is assumed to be small compared to both λ and λ_s. The SWs are thus almost electrostatic and propagate along the interface between the edge of the plasma and the dielectric tube [18]. The wave frequency ω is usually much larger than the ion plasma frequency so that the ions do not take part in the wave dynamics. The presence of the dielectric tube allows for better excitation and coupling conditions than that of pure metal chamber alone [7]. Furthermore, the metal screen reduces the outward radiation flux, thus enhancing the efficiency of plasma production [17].

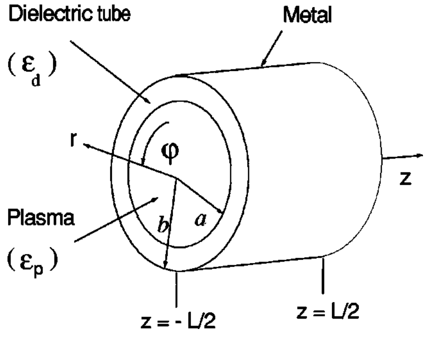

FIG. 1. Schematic diagram of a SW sustained discharge.

We shall use a warm-fluid description of the plasma. The electromagnetic fields of the SWs are calculated assuming that the chamber is uniformly filled with plasma with density equal to the spatially averaged plasma density $\overline{n}$. The validity of this approach has been discussed in earlier theoretical and experimental works [15,17]. The plasma is assumed to be uniform in the azimuthal direction and wave damping in that direction is neglected. The discharge is symmetrical with respect to plane $z=0$. The dependence of the electron temperature on the axial direction z is assumed to be weak. Furthermore, standing-wave effects in this direction are also neglected. The validity of our assumptions is discussed in Sec. V.

B. Wave electric fields

In the large plasma radius approximation ($a \gg \lambda, \lambda_s$), the radial electric field profiles of pure SWs in the plasma are [18]

$$E_\varphi \approx A \exp[-\kappa(a-r)]$$

and

$$E_r \approx i(k_\varphi/\kappa)E_\varphi, \tag{2}$$

where $\kappa^2=k_\varphi^2-(\omega/c)^2\varepsilon_p$, $\varepsilon_p=1-\omega_{pe}^2/\omega(\omega+i\nu_{en})$ is the dielectric constant of the uniform plasma, $\omega_{pe}=\sqrt{4\pi\overline{n}e^2/m_e}$ is the electron Langmuir frequency, and the field amplitude A can be obtained from the rf power absorbed by the plasma column. Here, ν_{en} is the electron-neutral collision frequency for momentum transfer, and e and m_e are the electron charge and mass, respectively. The propagation constant k_φ is obtained from the dispersion relation

$$\kappa\varepsilon_d+\varepsilon_p\kappa_d\tanh[\kappa_d(b-a)]=0, \tag{3}$$

where $\kappa_d^2=k_\varphi^2-(\omega/c)^2\varepsilon_d$, and ε_d and $b-a$ are the dielectric constant and thickness of the quartz tube, respectively.

The averaged plasma density will be computed from the particle and power balance equations and substituted into Eq. (3). The values of κ, κ_d, and k_φ are then obtained. The SW field distribution (2) is updated every time a change in $\overline{n}$ is detected.

C. Particle and power balance

As the column is uniform in the azimuthal direction, the problem is two dimensional (2D) and the plasma parameters depend on r and z only. It is assumed that the electron and ion energy distributions are Maxwellian with temperatures T_e and T_i, respectively. Furthermore, the ions and neutrals are kept at room temperature (300 K). For electrons the first three moments of the stationary Boltzmann equation are used, and for the ions the first two. For simplicity, the effects of impurities, such as dust and negative ions, are ignored. The overall charge neutrality condition is $n_e = n_i \equiv n$, where n_e and n_i are the equilibrium electron and ion densities, respectively.

We assume that the discharge operates in the ambipolar-diffusion regime, which is usually the case for low and intermediate pressures [19,20]. Accordingly, the particle balance equation for the electrons or ions is

$$\partial n/\partial t + \nabla \cdot (n\mathbf{v}) = n\nu^i, \tag{4}$$

where $\mathbf{v}$ is the electron or ion fluid velocity, and ν^i is the ionization rate. We recall that in the ambipolar diffusion-controlled regime [9]

$$\mathbf{v} \approx -\nabla(nT_e)/nm_i\nu_{\mathrm{in}},$$

where ν_{in} is the ion-neutral collision frequency, m_i is the ion mass, and $T_i \ll T_e$. We shall assume that $\nu_{in} = 2p_0$ [Torr] $\times 10^7$ s^{-1} is constant in the entire plasma column and is governed only by the gas pressure p_0 [21].

The rf power balance in the discharge is given by [19]

$$\frac{\partial nT_e}{\partial t} + \frac{2}{3}\nabla \cdot \mathbf{q}_e = -nI_e + S_{\mathrm{ext}}, \tag{5}$$

where I_e is the collision integral for the electrons, and $\mathbf{q}_e \approx -(5nT_e/2m_e\nu_{en})\nabla T_e$ is the heat flux density. The term S_{ext} denotes the rf power absorbed per unit volume by the plasma electrons, which for the present problem can be written as

$$S_{\mathrm{ext}} \approx (2/3)n\nu_{\mathrm{en}}m_e u_{\mathrm{osc}}^2,$$

where $u_{\mathrm{osc}} \approx (e^2|E_r^2 + E_\varphi^2|/2m_e^2\omega^2)^{1/2}$ is the time-averaged oscillation velocity of the plasma electrons [19]. The equilibrium state corresponds to setting $\partial_t = 0$ in Eqs. (4) and (5). The necessity of retaining the time-varying terms in the numerical computation is explained in the following section. The approach here is valid for fixed SW power absorption in the plasma column, with $Q = 2\int_0^{L/2}\int_0^a S_{\mathrm{ext}} 2\pi r\,dr\,z$, which also yields the constant A in Eq. (2). It is assumed that the electron-neutral collision frequency ν_{en} is constant. Its value for various parameter ranges is taken from the experiments [22].

If the excitation and ionization of the neutral gas is mainly by electron impact, the collision integral I_e is equal to the average power lost by an electron colliding with a neutral. Accordingly

$$I_e \approx (2m_e/m_n)T_e\nu_{\mathrm{en}} + \sum_j \nu_j\mathcal{E}_j + \nu^i\mathcal{E}^i,$$

where m_n is the mass of the neutral, ν_j is the excitation frequency from the ground state to level j with a threshold energy $\mathcal{E}_j$, and $\mathcal{E}^i$ is the ionization threshold. Stepwise ionization and excitation are neglected.

For argon gas, the rates for ionization and excitation to the states $4s$ and $4p$ are [23]

$$\nu^i = 8.13p_0 \times 10^8 T_e^{0.68}\exp(-\mathcal{E}_i T_e) \ \ \mathrm{s}^{-1},$$

$$\nu_{4s} = 1.77p_0 \times 10^8 T_e^{0.74}\exp(-\mathcal{E}_{4s} T_e) \ \ \mathrm{s}^{-1},$$

and

$$\nu_{4p} = 4.95p_0 \times 10^8 T_e^{0.71}\exp(-\mathcal{E}_{4p} T_e) \ \ \mathrm{s}^{-1},$$

where p_0 is in Torr, T_e in eV, $\mathcal{E}_i = 15.76$ eV, $\mathcal{E}_{4s} = 11.5$ eV, and $\mathcal{E}_{4p} = 13.2$ eV.

We now consider the boundary conditions for integrating Eqs. (4) and (5). Due to the symmetry, the radial gradients of the electron temperature and density are equal to zero at $r = 0$, and the axial gradients are equal to zero at $z = 0$. At the column edge ($r = a$) the radial component of the fluid velocity is assumed to satisfy the well-known Bohm sheath criterion $v_r(a,z) = \sqrt{T_e(a,z)/m_i}$ [9]. Similarly, at the side walls $z = \pm L/2$ we have $v_z(r, \pm L/2) = \sqrt{T_e(r, \pm L/2)/m_i}$. The boundary conditions for the heat flow are [19]

$$q_{er}(a,z) = T_e(a,z)(2 + \ln\sqrt{m_i/m_e})n(a,z)\sqrt{T_e(a,z)/m_i}$$

and

$$q_{ez}(r, \pm L/2) = T_e(r, \pm L/2)(2 + \ln\sqrt{m_i/m_e}) \times n(r, \pm L/2)\sqrt{T_e(r, \pm L/2)/m_i},$$

where q_{er} and q_{es} are the radial and axial components of the heat flux density.

III. THE 2D FLUID CODE

Equations (2)–(5) are solved numerically by integrating the governing dynamical equations in a self-consistent iterative manner. The numerical program consists of two blocks. The profiles of electron density, temperature, and fluid velocities are calculated in the first block. The resulting electron density distribution is used to compute the overall average plasma density $\overline{n}$, which is then used in the second program block to obtain the local values of the radial and azimuthal SW electric fields [normalized by $E_\varphi(a,0)$]. The computation is initialized using profiles of n, $\mathbf{v}$, and T_e estimated from less accurate analytical or computational results.

In the first program block, the nonlinear (with respect to n, T_e, and $\mathbf{v}$) Eqs. (4) and (5) are solved with the input parameters from Eqs. (2) and (3). However, using the so-called evolution (time-dependent) approach [24,25], one can effectively linearize the equations. The steady or equilibrium state is then obtained as a result of the time evolution of the system. This method is often used in the numerical solution of the stationary states of nonlinear evolution problems [24,25]. In fact, the nonlinear particle and power balance equations are replaced by linear ones with asymptotic solu-

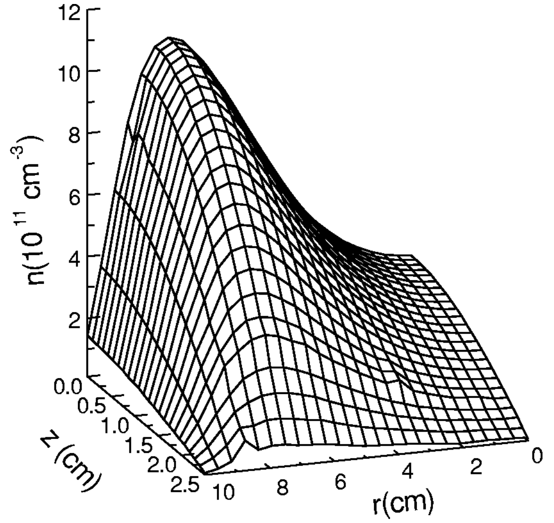

FIG. 2. 3D profiles of the plasma density in a 100 mTorr argon discharge in a dielectric tube with $\varepsilon_d = 4$, $a = 10$ cm, $b = 11.2$ cm, $L = 5$ cm sustained with 120-W rf power at 900 MHz.

tions coinciding with that of Eqs. (4) and (5) at steady state. The linearization is achieved by replacing the nonlinear term $\xi_j \zeta_j$, where ξ_j and ζ_j are any two plasma parameters taken at the jth step at time t_j, by $\xi_{j-1}\zeta_j$, where ξ_{j-1} is known from the last $(j-1)$th step of the calculation. The ionization, power absorption, and power loss terms on right-hand sides of Eqs. (4) and (5) are also evaluated using the values from the $(j-1)$th step. The linearized equations are then solved to obtain ζ_j. In this manner, all the plasma parameters are calculated at several subsequent time steps for the same SW field distribution. The calculation is terminated when the parameters no longer change noticeably with time, so that a steady state is reached. Using the steady-state profile of the electron number density, the spatially averaged value $\overline{n}$ is then computed straightforwardly. The latter is then substituted into Eqs. (2) and (3) (second program block) to obtain the updated SW field parameters. This computation cycle is repeated until both the plasma and field parameters no longer change with time. Clearly, the resulting equilibrium states are necessarily also dynamically stable. Further details of the numerical scheme are given in the Appendix.

IV. SPATIAL PROFILES OF PLASMA PARAMETERS

A. Short plasma cylinder $(a > L)$

We first consider the case when the axial dimension of the plasma is smaller than the radial one. We shall focus on the difference between SW plasmas with radial temperature gradient, as is the case in our simulation, and plasmas with uniform T_e. We shall refer to the latter case as ''uniform temperature plasma'' (UTP). The 3D density profile of a SW sustained plasma is shown in Fig. 2. One can notice that n is maximum near the discharge midplane $(z=0)$ and diminishes towards the axial walls at $z = \pm L/2$. In the radial direction, the plasma density clearly exhibits a maximum ≈6–7 cm away from the center. This profile is completely different from the UTP case shown in Fig. 3. The latter is within 3% of the solution consisting of the product of the radial Bessel profile (1) and the $\cos(\pi z/L)$ axial solution [9]. The small discrepancy can be attributed to the slightly different boundary conditions: the analytical solution is obtained assuming that the plasma density vanishes at the chamber walls, and in the computation the Bohm sheath criterion for the fluid fluxes on the walls is used.

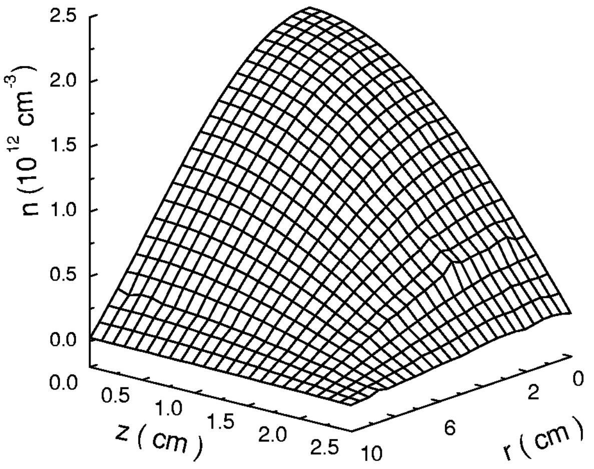

FIG. 3. Same as in Fig. 2, for a uniform temperature plasma.

From Figs. 2 and 3 one can see that the radial distribution of the plasma density in short cylindrical SW discharge differs considerably from that of the UTP. First, there is a large dip in the plasma density near the axis $(r=0)$, and it does not appear in the UTP. This profile is also different from that reported earlier for long cylindrical SW discharges [12,13,26]. In the latter case the maximum of the plasma density is near the axis $(r=0)$. However, in a short SW sustained discharge the maximum of n is closer to the discharge edge $r=a$.

Figure 4 shows the spatial profile of the electron temperature in a plasma column sustained by the SWs traveling along the cylinder circumference. Near the periphery of the discharge, T_e appears consistently higher than that for the UTP case. However, in the vicinity of the axis the tempera-

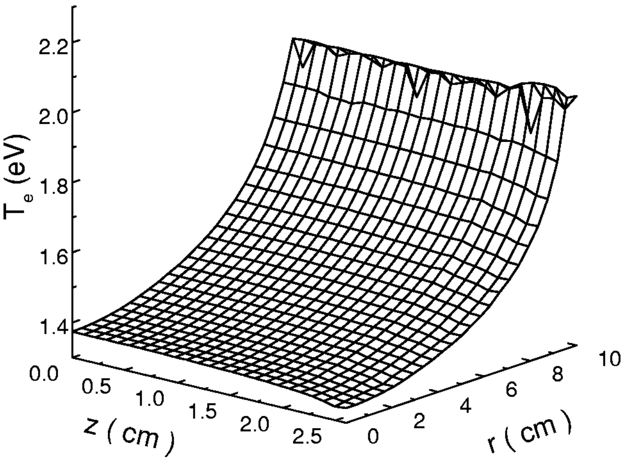

FIG. 4. Profiles of the electron temperature in the SW sustained discharge of Fig. 2.

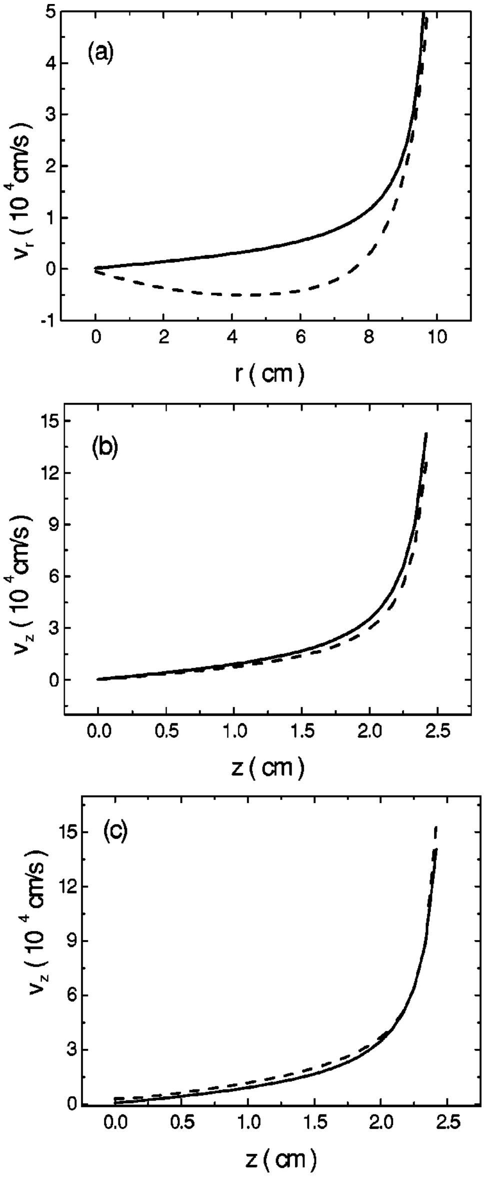

FIG. 5. Radial profiles at $z=0$ (a), axial at $r=0$ (b), and $r=a$ (c) of the fluid velocity for the parameters of Fig. 2. The dashed curves correspond to the SW sustained discharge and the solid curves are for the UTP.

ture (which can easily be obtained from the stationary form of the particle balance Eq. (4), as also discussed in [27]) of the UTP appears to be higher. This may be due to local power deposition by the edge-localized field of the *SW*s.

The radial profiles of the radial component of the ion velocity at $z=0$ are given in Fig. 5(a). Figures 5(b) and 5(c) illustrate the dependence on z of the axial velocity component near the discharge axis and edge, respectively. The solid curve corresponds to the UTP case. From Figs. 2–5 one can see that the distributions of the plasma parameters in the short cylindrical discharge are essentially different from that of a UTP. The most remarkable difference is in the radial fluid velocity [Fig. 5(a)]. The plasma parameters of the UTP case in Figs. 2–5 have been calculated for the same pressure, power absorption by the plasma, and discharge size as in case of SW sustained plasma.

Furthermore, as Fig. 5(a) suggests, in a plasma column with $a>L$, the fluid velocity in the discharge interior features a strong radial component. In fact, this is the case for $r\leqslant 0.75(a)$, where the electrons/ions move towards the center as well as drifting axially. It should be remarked that in contrast to the long cylindrical discharge case, here the particles recombine at the planar sidewalls $z=\pm L/2$. Hence, v_z does not vanish as is the case for long cylindrical SW discharges [12,13,26,28]. Meanwhile, recombination of particles at the discharge end walls also results in the diminishing of the plasma density near the axis (Fig. 2) of the short SW discharge. However, the axial profiles of the plasma density appear to be close to the conventional $\sim\cos(\pi z/L)$ profile. This can be attributed to the fact that the axial variation of the SW field and electron temperature profiles are weak and they do not noticeably affect the axial diffusion.

From Figs. 5(b) and 5(c) one can see that near the axis the axial electron/ion velocity is smaller than that in the UTP case. Conversely, near the plasma edge $r=a$, the opposite situation takes place. This can be explained by noting that in the discharge of our interest $T_e>T_e^{\mathrm{UTP}}$ near the edge, whereas $T_e<T_e^{\mathrm{UTP}}$ holds at $r=0$. Here, T_e^{UTP} is the electron temperature of the plasma with uniformly distributed temperature.

Variation of the power input also affects the plasma parameters, as depicted in Figs. 6(a)–6(c). Figure 6(a) shows the radial profiles of the plasma density for different powers absorbed by the plasma column. It is clearly seen that higher electron/ion number densities can be achieved by increasing the power input, which is a common feature of most of low-temperature plasmas [9]. In Figs. 6(b) and 6(c) the profiles of the electron temperature and nondimensional square of the total electric field $E_{\mathrm{tot}}^2=E_r^2+E_\varphi^2$ are shown. From Fig. 6(c) we see that an increase in the power absorbed by the plasma column results in a reduction of the SW field localization scale κ^{-1}. Specifically, κ^{-1} decreases from 0.94 cm to 0.53 cm while the power absorbed by the plasma electrons is elevated from 60 to 240 W. Hence it is expected that the electron temperature will increase in the vicinity of the dielectric boundary, as is confirmed by Fig. 6(b).

B. Plasma column with $2a\sim L$

We now turn our attention to the case when the chamber diameter and length are comparable $(2a\sim L)$. The discharge density profiles are presented in Fig. 7(a). One can see that the density minimum at the discharge center disappears. Moreover, the radial density profiles also differ essentially from that of the UTP case. In fact, the plasma profiles in the SW sustained discharge are flatter in the central part of the column and feature large shoulders, which is normally not the case for plasmas with uniformly distributed temperature. One also notices that the density shoulders become larger with increasing pressure, spanning about 80% of the cross section at $p_0=300$ mTorr. The radial profiles of the electron temperature under the same conditions are displayed in Fig. 7(b). It is seen that the average electron temperature decreases with pressure, but it becomes more nonuniform.

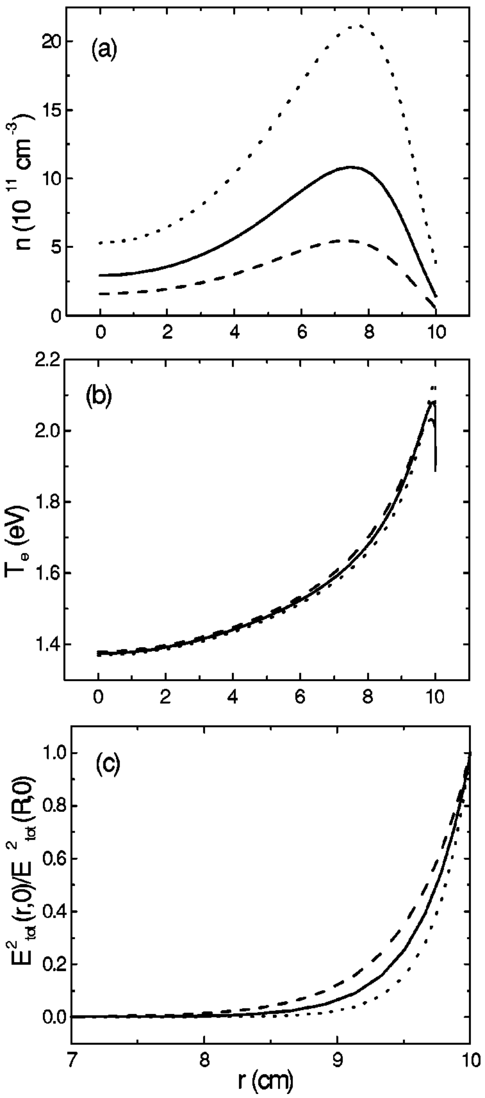

FIG. 6. Radial profiles of the plasma density (a), electron temperature (b), and $E_{\rm tot}^2(r,0)/E_{\rm tot}^2(R,0)$ (c), at $p_0=0.1$ Torr and $z=0$ for various powers absorbed in the plasma column. The dashed, solid, and dot curves correspond to 60, 120, and 240 W, respectively. The other conditions are the same as in Fig. 2.

Our results are compared with the experimental data from a discharge sustained by azimuthally travelling SWs in a metal-coated quartz cylindrical chamber with $2a\approx 12.6$ cm and $L\approx 14$ cm [15]. In this experiment, the plasma was generated by 500 W power microwaves at 2.45 GHz fed through a rectangular waveguide facing an axially aligned excitation slot in the metal at $\varphi=0$ [15]. The quartz tube has a permittivity $\varepsilon_d\approx 4$ and a thickness of 1.2 cm. The density and temperature profiles at the discharge midplane $z=0$ are obtained (Fig. 8) under the conditions of the experiment [15]. The curve 1 corresponds to the UTP case and features an almost constant temperature throughout the cross section. The curve 2 is the result from our model. One sees that our model yields a somewhat better agreement with the experiment than the UTP model. Possible reasons for the persisting discrepancy are discussed in the following section.

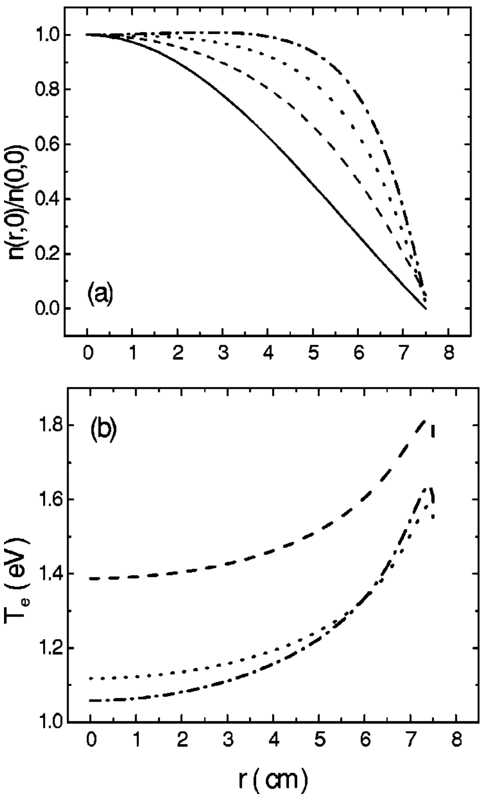

FIG. 7. Radial profiles at $z=0$ of the electron density (a) and temperature (b) in a vessel with $a=7.5$ cm, $b=8.7$ cm, and $L=15$ cm. The discharge is sustained with 120 W of rf power at 900 MHz. The dashed, dotted, and dash-dotted curves stand for $p_0=100$, 200, and 300 mTorr, respectively. In (a), $n(0,0)$ at 100, 200, and 300 mTorr is 1.73×10^{12}, 2.64×10^{12}, and 1.98×10^{12} cm^{-3}, respectively. The solid curve corresponds to the analytical solution (1).

V. DISCUSSION

In this section we shall discuss in more detail the relation between our model and the experiments of Refs. [15] and [4] (Sec. V A), the validity of the warm-fluid model used here (Sec. V B), and the possible causes of the quantitative discrepancies between the theoretical and experimental results pointed out in Sec. V C.

A. Excitation mechanisms of *SW* plasmas

We shall discuss briefly the various excitation mechanisms of SWs by the field applicator structures and their relation to our model. In microwave slot-excited plasmas, the slots of various configurations act as field applicators. Depending on the excitation conditions the power deposited to the plasma can either be localized in the vicinity of the slots, or be fairly uniformly distributed over the near-surface area. The details of the excitation conditions and properties of SW sustained plasmas can be found elsewhere [7]. In general, direct measurement of evanescent electric fields near the edge [29] is usually a fair indication of surface-wave excitation. Furthermore, when there were no SWs near the edge to create the plasma, the plasma particles there will diffuse to

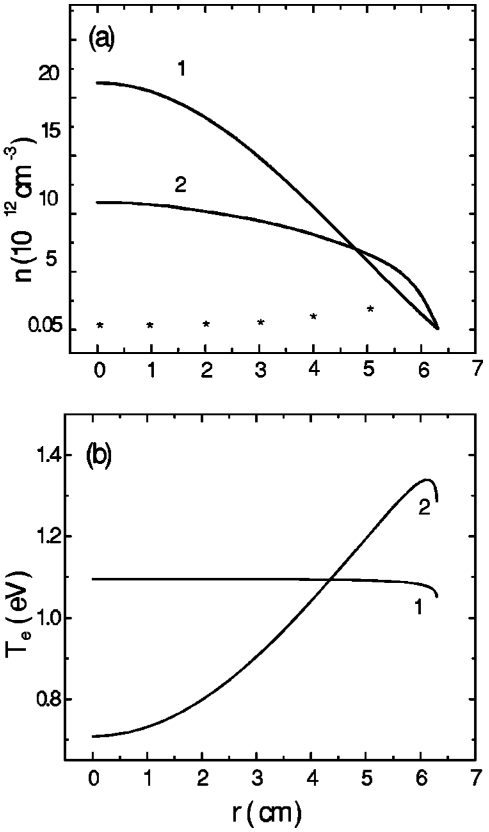

FIG. 8. Same as in Fig. 7 for $a = 6.3$ cm, $b = 7.5$ cm, $L = 14$ cm, $p_0 = 0.76$ Torr. The discharge is sustained with a rf power of $Q = 300$ W at 2.45 GHz. Curves 1 and 2 are for the UTP and SW sustained discharge, respectively. The experimental points are taken from Ref. [15].

the wall, and the density profile will be Bessel-like radially and cosinelike axially, as predicted by the diffusion equation (see also Sec. IV A). Hence, a careful analysis of the behaviors of the measured density and electromagnetic field profiles near the plasma edge is usually sufficient to conclude whether the plasma is SW driven or not [7].

The experiment of Ref. [15] features a single slot in a metal casing. The azimuthally traveling *SW*s are excited through the waveguide-facing axial slot in the metal enclosure of the quartz cylinder [15]. In this case the normalization constant $E_\varphi(a,0)$ used in our computation is the azimuthal component of the rf field near the wave exciting slot at $\varphi = 0$. In microwave slot-excited plasmas standing *SW*s with complex structure can be excited [7]. To avoid excitation of such standing waves, one can use another slot at the opposite end ($\varphi = \pi$) of the tube and excite simultaneously clockwise and counterclockwise propagating waves. In any case, if there were no azimuthally propagating *SW*s, one would have observed microwave field and the excited plasma localized near the slot. However, Viel *et al.* [15] report almost uniform azimuthal microwave field and plasma density profiles (Figs. 4, 8, 9 and 11 of Ref. [15]). Moreover, in Sec. IV B it has been shown that for the conditions of the experiment [15], azimuthally propagating *SW*s are indeed excited and are responsible for uniform azimuthal profile of the wave field and plasma density.

On the other hand, in the SLAN device [4] the plasma is sustained by axially nonsymmetric *SW*s propagating in the axial direction, with the electric field components of the form $\exp[i(k_3 z - \omega t)]\cos(m\varphi)$, where k_3 and m are the axial and azimuthal numbers. Long tubular SW sustained discharges sustained by axially propagating *SW*s have been well studied theoretically [11] and experimentally [30] for the $m = 1$ modes. Although the geometry of the SLAN system is close to that of Fig. 1, the SLAN experiments [4] feature multiple slots (e.g., $m = 10$ for SLAN II), where the field maxima occur. In this case wave excitation is only possible when the electron number density exceeds the critical value

$$n_{\min} = m_e \omega^2 (1 + \varepsilon_d)/(4\pi e^2),$$

which can be achieved only with sufficiently high input powers, since the latter must sustain the plasma density above the excitation threshold even at distances much larger than the wavelength from the field applicator [31]. When the *SW*s are excited, the plasma density profile in the SLAN system is linear in the axial direction. On the other hand, the appearance of cosinelike diffusive profiles (Fig. 12 of Ref. [4]) indicates the absence of SWs.

B. Validity of the warm-fluid description

There exist in the literature also kinetic, mostly 1D, models for discharge plasmas [28,32–35]. A kinetic approach would account for phenomena, such as collisionless wave damping and plasma heating, particle acceleration and trapping, etc. Most existing kinetic models are applicable in the collisionless or near collisionless regimes. In this paper we have adopted a warm-fluid approximation in a fully self-consistent nonlinear 2D model for describing the discharge. Many relevant works [13,25,36] have shown that the fluid approach is quite satisfactory for the pressure range ($\geqslant 100$ mTorr) of interest here. In this pressure range collisionless power absorption from nonlocal electron kinetic effects are weak compared to that of inelastic electron-neutral collisions [37,38]. In any case kinetic effects can only marginally affect the dispersion and field pattern of the SWs [39], since the wave phase velocity v_{ph} here is much larger the electron thermal speed v_{Te}. Note that the maximum value of v_{Te} here is 6×10^7 cm/s, whereas the minimum v_{ph} is 7×10^9 cm/s. Thus, accounting for kinetic effects in the discharge considered in the present problem would result in corrections that are of order v_{Te}/v_{ph} ($\ll 1$).

C. Possible causes of discrepancy between model and experiment

In Fig. 8(a), the discrepancy between the experimental [15] and computational results is quite large. A possible reason is that our code has been developed assuming diffusion-controlled particle loss, which is usually the case at low and intermediate pressures. In the pressure range 76–760 mTorr [15], volume recombination can become important and take part in the particle balance in the discharge. As a detailed study of the recombination processes is beyond the scope of

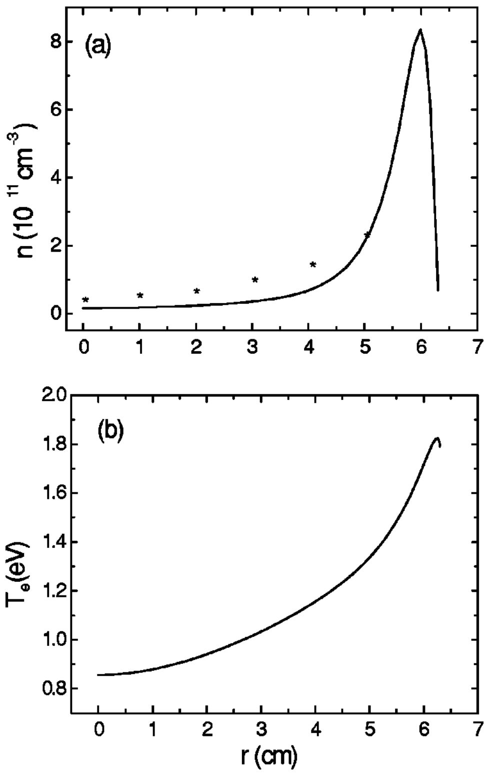

FIG. 9. Radial profiles of n (a) and T_e (b) in a SW discharge with the same parameters and experimental points as in Fig. 8, but accounting for volume recombination.

this work, we shall show by including a simple recombination term to the particle balance equations that the neglect of volume recombination can indeed be a reason for the discrepancy between our model and the experiment at higher pressures.

Accordingly, we add a term $\beta_r n^2$, where β_r is an effective coefficient of volume recombination, to the right-hand side of Eq. (4). Taking as typical value $\beta_r \sim 10^{-8}$ cm^3/s [40] and the parameters of the experiment [15], the radial profiles of the plasma density [Fig. 9(a)] and temperature [Fig. 9(b)] are computed. One can see that agreement between our model and the experiment is now significantly better. Furthermore, the typical values of the electron temperature are now higher than that shown in Fig. 8. Although the fairly good agreement with the experimental results seems to justify our simple recombination model, nevertheless the details of the recombination process should be included in order to make a more definitive conclusion.

There can also be other reasons for the quantitative discrepancy between our simulation and the experiment. For example, it is assumed in our model that the electron and ion elastic collision frequencies are constant throughout the plasma column, although ν_{en} and ν_{in} is weakly nonuniform. The existence of weak turbulence in the plasma can also make the diffusion process anomalous [41]. Likewise, the assumptions of uniform rf power deposition and neglect of axial electron and ion motion may also be somewhat oversimplified [15]. Furthermore, in the experiment it is difficult to estimate the exact value of rf power absorption by the plasma, and our model assumes that the power Q absorbed by the plasma electrons is equal to the power input through the waveguide. Finally, inaccuracies in the Langmuir probe measurements should also be mentioned [15].

VI. CONCLUSION

A theoretical model for short tubular discharges sustained by azimuthally traveling SWs has been developed. Using a 2D fluid code, stationary profiles of the plasma density, temperature, and fluid velocities have been computed. The numerical code developed here enables one to treat axial diffusion and radial nonuniformity of the electron temperature self-consistently. The resulting radial thermal fluxes are thus nonlinear. We have applied the model to rf discharges in LAR chambers. It is shown that the spatial structure of short tubular discharges differs essentially from that of long SW sustained plasma columns. In particular, in LAR chambers with $a > L$, dips in the plasma density near the axis frequently reported experimentally have been confirmed. The maximum of the electron/ion number density is shifted towards the discharge edge $r = a$. Furthermore, axial electron/ion motion can significantly affect the radial plasma density profiles. It is also shown that the radial fluid velocity is directed towards the axis. On the other hand, for discharges with $2a \sim L$ the radial plasma density profiles appear to be flatter and more uniform than that in UTPs. The uniformity improves with pressure. In particular, in argon discharge at 300 mTorr, one can expect generation of fairly flat density profiles over 80% of the chamber cross section.

The results obtained from the model are compared to available experimental data and fairly good agreement has been found. However, at higher pressures recombination in the plasma bulk appears to be essential and should be accounted for in improved models. In particular, it has been assumed that $\nu_{en} \ll \omega$, which is the case in the UHF and microwave ranges [9]. Thus, extension of our study to lower frequencies $\omega \sim \nu_{en}$ is warranted, and our results can be considered as a first step in obtaining fairly good quantitative agreement with that from the experiments.

The proposed model and its results suggest that radial uniformity of the plasma column can be efficiently controlled by varying the operating gas pressure [Fig. 7(a)]. Similarly, one expects that the width of the reported shoulders and the plasma density profiles can also be controlled by varying the rf power. The results also show that accounting for radial nonuniformity of the electron temperature and the corresponding heat flow yields a satisfactory explanation of the frequently reported deviations of the measured radial profile of the plasma density from that of Eq. (1). It may be of interest to point out that a shift of the maximum in the electron/ion number densities from the chamber center (Fig. 2) as predicted by the model has been observed recently also in inductively coupled plasmas with $R \sim L$ at lower frequencies [42]. This could be an intrinsic property of many LAR plasmas, so that our model with appropriate minor modifications may also be applicable to other LAR rf plasmas, especially when the rf power is deposited within a narrow layer near the column edge.

ACKNOWLEDGMENTS

This work was supported by the Science and Technology Center, Ukraine (Project No. 1112), the National Science and Technology Board of Singapore (Project No. 012 101 0024), SFB 191 Niedertemperatur Plasmen (Germany), the Australian Research Council, the Japan Society for the Promotion of Science, and NATO. Useful discussions with H. Sugai, R. Storer, and S. Xu are kindly appreciated. K.N.O. thanks H. Sugai for hospitality at Nagoya University, Japan.

APPENDIX: METHOD OF NUMERICAL SOLUTION

In our numerical solution, Eqs. (4) and (5) are first split into the two blocks. The first consists of

$$\frac{n_p-n_{p-1}}{t_p-t_{p-1}}+\frac{1}{r}\,\frac{\partial(rn_{p-1}v_{rp})}{\partial r}=(n\nu^i)_{p-1}-\frac{\partial(nv_z)_{p-1}}{\partial z}, \tag{A1}$$

$$\frac{U_p-U_{p-1}}{t_p-t_{p-1}}+\frac{2}{3r}\,\frac{\partial(r2q_{er})_p}{\partial r}=(-nI_e+S_{\text{ext}})_{p-1}, \tag{A2}$$

$$(v_r)_p\approx-(n_{p-1}m_i\nu_{in})^{-1}\partial U_p/\partial r, \tag{A3}$$

where $U=nT_e$, $(q_{er})_p=(5/2)[-U_{p-1}/(n_{p-1}m_e\nu_{en})\partial U_p/\partial r+(U^2)_{p-1}/(n^2m_e\nu_{en})_{p-1}\partial n_p/\partial r]$. The second block consists of

$$\frac{n_{p+1}-n_p}{t_{p+1}-t_p}+\frac{\partial n_p(v_z)_{p+1}}{\partial z}=(n\nu^i)_p-\frac{1}{r}\,\frac{\partial(rn_pv_{rp})}{\partial r}, \tag{A4}$$

$$\frac{U_{p+1}-U_p}{(t_{p+1}-t_p)}+\frac{2}{3}\,\frac{\partial(2q_{ez})_{p+1}}{\partial z}=(-nI_e+S_{\text{ext}})_p, \tag{A5}$$

$$(v_z)_{p+1}\approx(n_pm_i\nu_{in})^{-1}\partial U_{p+1}/\partial z, \tag{A6}$$

where $(q_{ez})_{p+1}=(5/2)[-U_p/(n_pm_e\nu_{en})\partial U_{p+1}/\partial z+(U^2/n^2m_e\nu_{en})_p\partial n_{p+1}/\partial z]$. The indices $p-1$, p, and $p+1$ correspond to the times t_{p-1}, t_p, and t_{p+1}, respectively.

The factors 2 in front of q_{er} and q_{ez} in Eqs. (A2) and (A5) have been inserted, since it is assumed that within the interval $\tau=t_p-t_{p-1}$ heat propagates only in the radial direction. The heat flowing through a unit surface in the r direction is then $2q_{er}\tau$. Similarly, during the (same) subsequent time interval $\tau=t_{p+1}-t_p$ heat propagates only in the z direction, with the corresponding flux $2q_{ez}\tau$ through a unit surface in z direction. Within the interval $2\tau=t_{p+1}-t_{p-1}$ the total heat flowing through a unit surface in the z and r directions is then $2(q_{er}+q_{ez})\tau$. Thus, the averaged heat flux density during 2τ is $q_{er}\mathbf{e}_r+q_{ez}\mathbf{e}_z$, which is the expression for heat flux density after Eq. (5).

The spatial profiles of the plasma parameters are computed as follows. We recall that n_{p-1}, $\mathbf{v}_{p-1}$, and U_{p-1} are the output of the previous step (time t_{p-1}). The absorbed power density $(S_{\text{ext}})_{p-1}=n_{p-1}\nu_{en}E_{\text{eff}}^2B$ entering Eq. (5) depends on the constant B, which is yet to be defined. Here, $E_{\text{eff}}^2=|E_r^2(r,z)+E_\varphi^2(r,z)|/E_\varphi^2(a,0)$, and $B=e^2E_\varphi^2(a,0)/(3m_e\omega^2)$. Assuming that the total power absorbed by the plasma column

$$Q=2\int_0^{L/2}\int_0^a n_{p-1}\nu_{en}E_{\text{eff}}^2B2\pi r\,dr\,dz$$

is fixed, one immediately obtains $B=Q/(2\int_0^{L/2}\int_0^a n_{p-1}\nu_{en}E_{\text{eff}}^2 2\pi r dr dz)$, whereupon B is substituted in $(S_{\text{ext}})_{p-1}$. The solution of the linear set (A1)–(A3) yields the values of n, v_r, and U at $t_p=t_{p-1}+\tau$.

Substituting n_p, $(v_r)_p$, and U_p into Eqs. (A4)–(A6), one then computes n_{p+1}, $(v_z)_{p+1}$, and U_{p+1}, corresponding to the time $t_{p+1}=t_p+\tau$. Assuming $n_{p-1}=n_{p+1}$, $(v_z)_{p-1}=(v_z)_{p+1}$, and $U_{p-1}=U_{p+1}$, one obtains the discharge parameters at t_p and t_{p+1}. This procedure for computing n, v_r, v_z, U is repeated with the same electric field until the profiles become constant in time. We have then obtained the steady-state profiles of the electron density, fluid velocity, and temperature, corresponding to the given, or current, rf field distribution. The electron density is then spatially averaged to obtain $\tilde{n}$. Using the value of the average plasma density $\overline{n}$, new distributions of the normalized SW electric field in the plasma column are obtained. The entire cycle is repeated until again the density and field profiles no longer change with iteration.

The difference scheme approximating the particle and power balance Eqs. (A1) and (A2) was obtained using the balance (integrointerpolation) method [24,43]. The interval $[0,\ a]$ was divided into m segments, with the edge coordinates $r(i)=a\sin[\pi(i-1)/2m]$, where $i=1,2,...,m+1$. This enables one to concentrate the iteration points near the radius where the SW electric field changes most rapidly. Analogously, the interval $[0,L/2]$ was divided on k segments. To obtain the spatial distribution of the discharge parameters, n and U were calculated at $(r(i),z(j))$, where $j=1,2,...,k+1$. The values of v_r and v_z were computed at $([r(i)+r(i+1)]/2,z(j))$ and $(r(i),[z(j)+z(j+1)]/2)$, respectively. Equations (A1) and (A2) were multiplied by $2\pi r dr dz$ and integrated over the radius from $r(1)=0$ to $[r(1)+r(2)]/2$, then from $[r(1)+r(2)]/2$ to $[r(3)+r(2)]/2$,..., again from $[r(m-1)+r(m)]/2$ to $[r(m+1)+r(m)]/2$, and eventually from $[r(m+1)+r(m)]/2$ to $r(m+1)=a$. Similarly, integration of the equations over the axial intervals $(z(1)=0,[z(1)+z(2)]/2)$, $([z(1)+z(2)]/2,[z(3)+z(2)]/2),\dots,$ $([z(k-1)+z(k)]/2,[z(k+1)+z(k)]/2)$, and $([z(k+1)+z(k)]/2,z(k+1)=L/2)$ has been performed. In this way, the set of $2(m+1)(k+1)$ equations with the $2(m+1)(k+1)$ unknown values of $n_p(i,j)$ and $E_p(i,j)$ is generated from Eqs. (A1) and (A2).

Because of symmetry, we assumed $v_r=0$ and $q_{er}=0$ on the plasma column axis $(r=0)$. Integration from $[r(m+1)+r(m)]/2$ to a requires the linearized boundary conditions for the electron/ion and heat fluxes at $r=a$

$$[n(a,z)v_r(a,z)]_p=(2\sqrt{m_i})^{-1}[U_p(a,z)\,\eta_{p-1}+n_p(a,z)\,\eta_{p-1}^{-1}],$$

$$[q_{er}(a,z)]_p=[2+\ln\sqrt{m_i/m_e}]/(2\sqrt{m_i})\times[3U_p(a,z)\,\eta_{p-1}^{-1} - n_p(a,z)\,\eta_{p-1}^{-3}],$$

where $\eta_{p-1}=\sqrt{[n(a,z)/U(a,z)]_{p-1}}$.

Equation (A3) for the fluid velocity was not integrated. The value of $(v_r)_p$ was found at the following points: $([r(1)+r(2)]/2,z(j))$, $([r(3)+r(2)]/2,z(j)),\ldots,$ $([r(m+1)+r(m)]/2,z(j))$, where $j=1,2,\ldots,k+1$. Thus, there are $m(k+1)$ values of $(v_r)_p$ to be found. In the discharge center $(r=0)$, $v_r=0$, while at $r=a$ the radial component of the charged particle velocity is equal to the ion acoustic velocity. To find $(v_r)_p$ at the above points, the following $m(k+1)$ difference equations have been obtained from Eq. (A3):

$$[v_r(i,j)]_p=-2/\{m_i\nu_{in}[n_{p-1}(i+1,j)+n_{p-1}(i,j)]\}\times[U_p(i+1,j)-U_p(i,j)]/[r(i+1,j)-r(i,j)],$$

where $i=1,2,\ldots,m$, $v_r(i,j)$ is the fluid velocity at $([r(i)+r(i+1)]/2,z(j))$, and $n(i,j)$ and $U(i,j)$ are the corresponding values at $(r(i),z(j))$.

Eventually, from Eqs. (A1)–(A3), the set of $(3m+2)(k+1)$ linear equations with the same number of variables has been obtained. The linearized set corresponding to Eqs. (A4)–(A6) can be derived similarly.

The boundary conditions for $(v_z)_{p+1}$ and $(q_{ez})_{p+1}$ at $z=L/2$ at any radial position are

$$[n(r,L/2)v_z(r,L/2)]_{p+1}=(2\sqrt{m_i})^{-1}[U_{p+1}(r,L/2)\,\delta_p + n_{p+1}(r,L/2)\,\delta_p^{-1}],$$

$$[q_{ez}(r,L/2)]_{p+1}=[2+\ln\sqrt{m_i/m_e}]/(2\sqrt{m_i})\times[3U_{p+1}(r,L/2)\,\delta_p^{-1} - n_{p+1}(r,L/2)\,\delta_p^{-3}],$$

where $\delta_p=\sqrt{[n(r,L/2)/U(r,L/2)]_p}$. By symmetry, for any radial coordinate, v_z and q_{ez} are assumed to vanish at $z=0$. Finally, the linearized equations were solved by the Gauss method.

[1] *Plasma-Surface Interactions and Processing of Materials*, edited by O. Auciello, A. Gras-Marti, J. A. Valles-Abarca, and D. L. Flamm (Kluwer Academic, Boston, 1990).

[2] *Advanced Technologies Based on Wave and Beam Generated Plasmas*, NATO Advanced Studies Institute Partnership Subseries 3, edited by H. Schlueter and A. Shivarova (Kluwer, Amsterdam, 1999).

[3] *Microwave Discharges: Fundamentals and Applications*, Vol. 302 of *NATO Advanced Studies Institute, Series B: Physics*, edited by C. M. Ferreira and M. Moisan (Plenum, New York, 1993).

[4] D. Korzec, F. Werner, R. Winter, and J. Engemann, Plasma Sources Sci. Technol. **5**, 216 (1996).

[5] G. Sauve, M. Moisan, R. Grenier, and Z. Zakrzewski, J. Microwave Power Electromagn. Energy **30**, 58 (1995).

[6] T. Ikushima, Y. Okuno, and H. Fujita, Appl. Phys. Lett. **64**, 25 (1994).

[7] H. Sugai, I. Ghanashev, and M. Nagatsu, Plasma Sources Sci. Technol. **7**, 192 (1998).

[8] S. Xu, K. N. Ostrikov, W. Luo, and S. Lee, J. Vac. Sci. Technol. A **18**, 2185 (2000).

[9] M. A. Lieberman and A. J. Lichtenberg, *Principles of Plasma Discharges and Materials Processing* (Wiley, New York, 1994).

[10] A. L. Vikharev, O. A. Ivanov, and A. L. Kolisko, Tech. Phys. Lett. **22**, 832 (1996).

[11] I. Zhelyazkov and V. Atanassov, Phys. Rep. **255**, 79 (1995).

[12] C. M. Ferreira, J. Phys. D **14**, 1811 (1981).

[13] I. Peres, M. Fortin, and J. Margot, Phys. Plasmas **3**, 1754 (1996).

[14] L. St-Onge, J. Margot, and M. Chaker, Plasma Sources Sci. Technol. **7**, 154 (1998).

[15] V. Viel, J. Bernard, and G. Laval, J. Phys. D **29**, 1500 (1996).

[16] G. DiPeso, T. D. Rognlien, V. Vahedi, and D. Hewett, IEEE Trans. Plasma Sci. **23**, 550 (1995).

[17] E. L. Tsakadze, K. N. Ostrikov, S. Xu, I. R. Jones, R. Storer, M. Y. Yu, and S. Lee, Phys. Rev. E **63**, 046402 (2001); E. L. Tsakadze, K. N. Ostrikov, S. Xu, R. Storer, and H. Sugai, J. Appl. Phys. **91**, 1804 (2002).

[18] N. A. Azarenkov and K. N. Ostrikov, Phys. Rep. **308**, 333 (1999).

[19] V. E. Golant, A. P. Zhilinskii, and I. E. Sakharov, *Fundamentals of Plasma Physics* (Wiley, New York, 1980).

[20] T. Petrova, E. Benova, G. Petrov, and I. Zhelyazkov, Phys. Rev. E **60**, 875 (1999).

[21] S. C. Brown, *Introduction to Electrical Discharges in Gases* (Wiley, New York, 1966).

[22] Z. Zakrzewski, M. Moisan, V. M. M. Glaude, C. Beudry, and P. Leprince, Plasma Phys. **19**, 77 (1977).

[23] S. Ashida, C. Lee, and M. A. Lieberman, J. Vac. Sci. Technol. A **13**, 2498 (1995).

[24] S. K. Godunov and V. S. Ryabenkii, *Difference Schemes: An Introduction to Underlying Theory* (North-Holland, Amsterdam, 1987).

[25] H. M. Wu, B. W. Yu, A. Krishnan, M. Li, Y. Yang, J. P. Yan, and D. P. Yuan, IEEE Trans. Plasma Sci. **25**, 776 (1997).

[26] N. A. Azarenkov, I. B. Denysenko, A. V. Gapon, and T. W. Johnston, Phys. Plasmas **8**, 1467 (2001).

[27] F. Vidal, T. W. Johnston, J. Margot, M. Chaker, and O. Pauna, IEEE Trans. Plasma Sci. **27**, 727 (1999).

[28] Yu. M. Aliev, A. V. Maximov, U. Kortshagen, H. Schlueter, and A. Shivarova, Phys. Rev. E **51**, 6091 (1995).

[29] H. Sugai, I. Ghanashev, M. Hosokawa, K. Mizuno, K. Nakamura, H. Toyoda, and K. Yamauchi, Plasma Sources Sci. Technol. **10**, 378 (2001).

[30] J. Margot-Chaker, M. Moisan, M. Chaker, V. M. M. Glaude, P. Lauque, J. Paraszczak, and G. Sauve, J. Appl. Phys. **66**, 4134 (1989).

[31] A. W. Trivelpiece and R. W. Gould, J. Appl. Phys. **30**, 1784 (1959).

[32] V. I. Kolobov and V. A. Godyak, IEEE Trans. Plasma Sci. **23**, 503 (1995).

[33] U. Kortshagen, C. Busch, and L. D. Tsendin, Plasma Sources Sci. Technol. **5**, 1 (1996).

[34] C. M. Ferreira and J. Loureiro, Plasma Sources Sci. Technol. **9**, 528 (2000).

[35] M. Shoucri, A. Cote, C. Cote, G. Pacher, P. Matte, A. Cardinali, and R. Spigler, Bull. Am. Phys. Soc. **46**(8), 169 (2001).

[36] R. A. Stewart, P. Vitello, D. B. Graves, E. F. Jaeger, and L. A. Berry, Plasma Sources Sci. Technol. **4**, 36 (1995).

[37] M. M. Turner, Phys. Rev. Lett. **71**, 1844 (1993).

[38] V. A. Godyak and V. I. Kolobov, Phys. Rev. Lett. **79**, 4589 (1997).

[39] N. A. Krall and A. W. Trivelpiece, *Principles of Plasma Physics* (Mc Graw-Hill, New York, 1973).

[40] L. M. Biberman, V. S. Vorob'ev, and I. T. Yakubov, *Kinetics of Non-Equilibrium Low-Temperature Plasma* (Nauka, Moscow, 1982), in Russian.

[41] C. M. Ryu and M. Y. Yu, Phys. Scr. **57**, 601 (1998).

[42] K. N. Ostrikov, S. Xu, and A. B. M. Shafiul Azam, J. Vac. Sci. Technol. A **20**, 251 (2002); A. B. M. Shafiul Azam, E. L. Tsakadze, Y. Li, K. N. Ostrikov, S. Xu, and S. Lee, Bull. Am. Phys. Soc. **45**(7), 148 (2000).

[43] A. N. Tikhonov and A. A. Samarskii, *Partial Differential Equations of Mathematical Physics* (Holden-Day, San Francisco, 1967).